Monthly Notices
of the
ROYAL ASTRONOMICAL SOCIETY

MNRAS **448,** 1945–1955 (2015) doi:10.1093/mnras/stu2680

Orbital and physical parameters of eclipsing binaries from the ASAS catalogue – VIII. The totally eclipsing double-giant system HD 187669*

K. G. Hełminiak,[1,2]† D. Graczyk,[3,4]‡ M. Konacki,[2,5] B. Pilecki,[4,6] M. Ratajczak,[2] G. Pietrzyński,[4,6] P. Sybilski,[2] S. Villanova,[4] W. Gieren,[3,4] G. Pojmański,[6] P. Konorski,[6] K. Suchomska,[6] D. E. Reichart,[7] K. M. Ivarsen,[7] J. B. Haislip[7] and A. P. LaCluyze[7]

[1]*Subaru Telescope, National Astronomical Observatory of Japan, 650 North Aohoku Place, Hilo, HI 96720, USA*
[2]*Nicolaus Copernicus Astronomical Center, Department of Astrophysics, ul. Rabiańska 8, PL-87-100 Toruń, Poland*
[3]*Millenium Institute of Astrophysics, Av. Vicuña Mackenna 4860, Santiago, Chile*
[4]*Universidad de Concepción, Departamento de Astronomía, Casilla 160-C, Concepción, Chile*
[5]*Astronomical Observatory, A. Mickiewicz University, ul. Słoneczna 36, PL-60-286 Poznań, Poland*
[6]*Warsaw University Observatory, Al. Ujazdowskie 4, PL-00-478 Warsaw, Poland*
[7]*Department of Physics, and Astronomy, University of North Carolina, Campus Boc 3255, Chapel Hill, NC 27599-3255, USA*

Accepted 2014 December 15. Received 2014 December 14; in original form 2014 June 26

ABSTRACT

We present the first full orbital and physical analysis of HD 187669, recognized by the All-Sky Automated Survey (ASAS) as the eclipsing binary ASAS J195222-3233.7. We combined multi-band photometry from the ASAS and SuperWASP public archives and 0.41-m PROMPT robotic telescopes with our high-precision radial velocities from the HARPS spectrograph. Two different approaches were used for the analysis: (1) fitting to all data simultaneously with the WD code and (2) analysing each light curve (with JKTEBOP) and radial velocities separately and combining the partial results at the end. This system also shows a total primary (deeper) eclipse, lasting for about 6 d. A spectrum obtained during this eclipse was used to perform atmospheric analysis with the MOOG and SME codes to constrain the physical parameters of the secondary. We found that ASAS J195222-3233.7 is a double-lined spectroscopic binary composed of two evolved, late-type giants, with masses of $M_1 = 1.504 \pm 0.004$ and $M_2 = 1.505 \pm 0.004$ $M_\odot$, and radii of $R_1 = 11.33 \pm 0.28$ and $R_2 = 22.62 \pm 0.50$ $R_\odot$. It is slightly less metal abundant than the Sun, and has a $P = 88.39$ d orbit. Its properties are well reproduced by a 2.38-Gyr isochrone, and thanks to the metallicity estimation from the totality spectrum and high precision of the masses, it was possible to constrain the age down to 0.1 Gyr. It is the first so evolved Galactic eclipsing binary measured with such good accuracy, and as such it is a unique benchmark for studying the late stages of stellar evolution.

Key words: binaries: eclipsing – binaries: spectroscopic – stars: evolution – stars: fundamental parameters – stars: individual: HD 187669 – stars: late-type.

1 INTRODUCTION

Despite the fortunate configuration of detached eclipsing binaries (DEBs) and the many possibilities that they give us, analysis of these objects is still difficult. The light curves do not contain enough information about the effective temperatures in the absolute scale, mainly their ratio. They are sometimes set on the basis of the colour of the whole system, which is the combined light of two, sometimes very different stars. Another problem occurs when calculating the fractional radii (defined as a fraction of the major semi-axis). The information about their sum comes mainly from the width of eclipses, and is somewhat degenerated with the inclination angle, but from the light curves only it is difficult to constrain their ratio. Again, other kinds of data are needed, like spectra, from which one can try to estimate the ratio of fluxes from the two components. Both issues are, however, much less important in even more fortunate cases when a system shows total eclipses, when light from only one component is seen. A flat minimum in the light curves solves these problems and other kinds of observation can help to improve the analysis even more.

* Based on observations collected at the European Southern Observatory, Chile under programmes 085.C-0614, 085.D-0395, 086.D-0078, 087.C-0012, 089.C-0415, 190.D-0237 and 091.D-0469.

†Subaru Research Fellow, E-mail: xysiek@naoj.org
‡E-mail: darek@astro-udec.cl

Such a fortunate situation occurs either when the inclination angle is very close to 90 degrees, or when the two stars have significantly different sizes. The latter usually means that at least one component is evolved. Because of the long-lasting evolution on the main sequence, such evolved systems are much less common than main-sequence eclipsing binaries. In a very fine summary, Torres, Andersen & Gimenez (2010) point out the lack of red giant systems with accurately measured properties, especially masses and radii. Torres et al. (2010) list only four red giants in their sample: AI Phe A, TZ For A, and both components of OGLE-051019.64-685812.3 in the Large Magellanic Cloud (LMC). Since then a small number of systems have been added to the sample, but either containing one giant component (KIC 8410637; Frandsen et al. 2013), or located in the Magellanic Clouds (e.g. Pietrzyński et al. 2013; Graczyk et al. 2014), i.e. no Galactic double-giant system has been accurately studied. Some interesting cases have been analysed (Gałan et al. 2008; Ratajczak et al. 2013), but for various reasons their parameters have not yet been determined precisely enough. Long baseline interferometry has been successful in measuring the radii of single red giants directly, but without mass determination. Asteroseismology of solar-type oscillations is another option, and with the long-cadence, continuous and precise light curves from the *CoRoT* and *Kepler* satellites, it appears to be a promising method (Kallinger et al. 2009; Bedding et al. 2010), especially if combined with interferometric radius measurements (Baines et al. 2014), but still the precision achieved is lower than for double-lined DEBs, or the differences between the parameters obtained from asteroseismology and other methods is significant.

In this paper we present our results of a detailed analysis of a binary system showing a total eclipse, and composed of two cool giant stars – ASAS J195222-3233.7 (HD 187669, CD-32 15534, TYC 7443-867-1; hereafter ASAS-19). Despite being relatively bright – $V \sim 8.9$ mag – this star was recognized as a binary only in the All-Sky Automated Survey (ASAS; Pojmański 2002)[1] and this is the first detailed study of this interesting target. Time-series photometry is also available in the Public Archive of the Wide-Angle Search for Planets (SuperWASP; Pollacco et al. 2006). Except for single-epoch brightness and position measurements, no information is available in other databases or the literature. The only spectral type classification – K0III – is from Houk (1982).

Two teams were working on this system mostly independently. One group was led by KH (the H-group with MK, MR and PS) and the second group by DG (the G-group with BP, GP, PK, SV, WG and KS). We used the same data in our analyses and we compared our partial results as the work progressed. However, the overall approach used by each group was different. In the end, we combined our results to obtain the final parameters of the system.

2 OBSERVATIONS

2.1 Photometry

2.1.1 ASAS

The *V*-band photometry of ASAS-19, publicly available from the ASAS Catalogue,[2] spans from 2000 November to 2009 December, and contains 406 good quality points (flagged A in the original data).

[1] http://www.astrouw.edu.pl/asas/?page=acvs
[2] http://www.astrouw.edu.pl/asas/?page=aasc

Table 1. The PROMPT *V*, *I* and ASAS *I* photometry of ASAS-19. Portion of the table is shown for the reference. The complete table is available in the online version of the manuscript.

BJD-2450000	Mag	Error	Set
2404.777 62	7.567	0.075	AI
2405.806 52	7.480	0.071	AI
2406.820 07	7.502	0.074	AI
2415.822 23	7.494	0.068	AI
2500.621 85	7.533	0.074	AI
...			

The *I*-band photometry was downloaded from the internal ASAS catalogue and spans from 2000 May to 2009 June, and contains 247 good points.

2.1.2 SuperWASP

From the SuperWASP public archive,[3] we extracted raw flux measurements of the binary. To transform them to magnitudes, we used flux measurements of a nearby, slightly brighter star HD 187742 ($V = 8.07$ mag, $SW = 8.193$ mag), also classified as K0III (Houk 1982), which we previously inspected for variability. We cross-matched the two data sets and removed the obvious outliers from the resulting light curve. Originally, the SuperWASP data spanned from 2006 March to 2008 May (three observing seasons), but we found that the data from 2007 and 2008 suffer from large systematic variations, thus we decided to include data only from 2007 April and July, when the primary eclipse was recorded, and the observations do not have significant outliers. We ended up with 5554 good data points.

2.1.3 PROMPT

Dedicated photometric observations of ASAS-19 were carried out for the *V* and *I* bands with the 0.41-m Prompt-4 and Prompt-5 robotic telescopes,[4] located in the Cerro Tololo Inter-American Observatory in Chile. A more detailed description of the observational settings, reduction procedure and calibration to a standard photometric system can be found in Hełminiak et al. (2011). The PROMPT observations span about 400 d. In total, we secured 1714 and 1400 measurements for the *V* and *I* bands, respectively. The typical exposure times were 5–7 s for the *V* band and 2–3 s for the *I* band. Most of the observations were concentrated in the two eclipses, especially in the flat part of the primary one, which was covered almost completely by both bands between 2009 September 20 and 25.

Table 1 contains PROMPT *V*-band and *I*-band, and ASAS *I*-band light curves. The first column is the time stamp BJD-2450000. The second and third columns are the measured brightness (in mag) and its formal error. The last column denotes the data set: AI = ASAS *I*, PI = PROMPT *I*, and PV = PROMPT *V*. The complete table is

[3] http://exoplanetarchive.ipac.caltech.edu/applications//ExoTables/search.html?dataset=superwasptimeseries
[4] Panchromatic Robotic Optical Monitoring and Polarimetry Telescopes. PROMPT is operated by SKYNET (http://skynet.unc.edu) – a distributed network of robotic telescopes located around the world, dedicated to continuous gamma-ray burst afterglow observations.

available in machine-readable form in the electronic version of the manuscript.

2.2 HARPS spectroscopy

ASAS-19 was observed spectroscopically with the High Accuracy Radial velocity Planet Searcher (HARPS; Mayor et al. 2003), attached to the 3.6-m telescope in La Silla Observatory, Chile, between 2010 August and 2013 June. A total of 27 spectra were taken in two modes – high efficiency (EGGS) and high radial velocity (RV) accuracy.

14 spectra, taken between 2009 and 2013, were obtained in the high-efficiency EGGS mode. The exposure time was usually between 300 and 600 s depending on seeing conditions at La Silla. We would like to draw special attention to the spectrum from 2010 September 10, taken exactly during the total part of the primary eclipse, when light from only one component was recorded. This spectrum was used for atmospheric analysis, but the RV was not measured.

13 spectra, taken between 2011 June and 2012 September, were obtained in the high RV accuracy mode. The exposure time for those observations varied between 780 and 1200 s, giving a signal-to-noise ratio (S/N) around 5500 Å of 70–120. All spectra were reduced on-site with the available Data Reduction Software (DRS).

3 ANALYSIS

3.1 Radial velocities

3.1.1 H-group

RVs were initially calculated with the two-dimensional cross-correlation TODCOR code (Zucker & Mazeh 1994), with synthetic spectra taken as templates. These RVs were then used as starting values for the tomographic spectral disentangling and least-squares fitting procedure (Konacki et al. 2010). This procedure uses tomographic methods to produce decomposed spectra of each star, suitable for more precise RV measurements and spectral analysis (after proper scaling). To find the new RVs, the code uses the least-squares method to find shifts of the two spectra in the log λ domain, so their sum matches a given observed spectrum.

3.1.2 G-group

The components' RVs were determined using the RaVeSpAn code (Pilecki, Konorski & Górski 2012) utilizing the broadening function formalism (Rucinski 1992, 1999). We used templates from the synthetic library of local thermodynamic equilibrium (LTE) spectra by Coehlo et al. (2005); the templates were not convolved down to the HARPS resolution. In the beginning, we choose templates to match the components' effective temperature, gravity and abundance. However, the resulting rms values of both RV curves were significantly larger than those from the H-group. We decided to investigate the effect. It turned out that using solar metallicity and a cooler template ($T_{\rm eff} \approx 4000$ K) for both components reduced rms values by a factor of 1.5. Further, the difference in rms values between both stars was reduced to almost zero, signifying similar precision of their RV determination. We expected this because although the secondary rotates twice as fast as the primary (producing larger rotational broadening of lines), at the same time it is optically 2.5 times brighter (producing significantly stronger lines in the combined spectrum). These effects should cancel out if there are no other important sources of scatter (i.e. stellar spots). The resulting RVs have slightly larger rms values than those derived by tomographic spectral disentangling. Also, the γ difference between components is much smaller –40 m s^{-1} – and comparable with individual rms values (see later sections). The overall precision of RV measurements and orbital solutions made by both groups is slightly worse than expected from the spectrograph performance. This is probably because of a noticeable rotational broadening of both components and/or stellar activity. Our measurements and their residuals from the WD fit are shown in Table 2.

3.2 Spectroscopic orbital fit (H-group)

The strategy of the H-group was to obtain partial results with different approaches and working on different data, and combine them into one set later. The orbital fit to the RVs measured by least-squares fitting was done first. The fit was performed with the V2FIT code, which is a simple procedure that fits a double-Keplerian solution with a Levenberg–Marquardt algorithm. As free parameters, we set the two velocity semi-amplitudes $K_{1,2}$, orbital period P, centre-of-mass velocity of the primary γ_1, the difference between the two centre-of-mass velocities $\gamma_2 - \gamma_1$, and the time of phase zero, defined as the moment of the periastron passage for eccentric orbits, or a quadrature for circular orbits. Initially we also set as free the eccentricity e and argument of the periastron ω, but we found e to be indifferent from zero.

We found, however, that the two components have significantly different values of γ, with the primary's (defined here as the hotter star) being blue-shifted by 177 ± 15 m s^{-1} – larger than that found by the G-group. Several explanations are possible, but the one we find the most plausible is that it is a systematic difference introduced by the method used by the H-group, which is optimized for precise measurements of velocity variations, not their absolute values. We also find it possible that it was due to stellar spots, which caused time-varying asymmetries in line profiles, which finally led to a template mismatch, or due to different large-scale convective motions in the two stars (Schwarzschild 1975; Porter & Woodward 2000). We can exclude the differential gravitational red shift, as it would make the secondary blue-shifted.

The measurement errors of the order of single m s^{-1} appear to be underestimated, so to get the reduced χ^2 close to 1, and thus reliable statistical errors of the parameters, we added in quadrature a systematic contribution of 36 and 52 m s^{-1} for the primary and secondary, respectively. To account for possible systematic differences in the final solution, we ran 10 000 Monte Carlo iterations, perturbing the parameters that were held fixed (i.e. e and ω). We added the Monte Carlo errors to the statistical ones in quadrature; however, they were typically an order of magnitude lower than the statistical ones. All the RV measurements from the tomographic disentangling, together with their residuals from the model RV curve, are shown in Table 2. Neither of the groups used the spectrum taken in totality for the RV calculations and further modelling. The resulting orbital parameters are presented in Table 3, and the corresponding model RV curves are shown in Fig. 1.

3.3 Spectral analysis of the decomposed and total eclipse spectra

3.3.1 MOOG (G-group)

We disentangled the spectra of both components and then we analysed them together with the single spectrum of the secondary

Table 2. Radial velocity measurements from disentangling and least-squares spectra fitting (H-group), and RaVeSpAn (G-group), and their residuals (all in km s^{-1}). Index 1 denotes the hotter star (primary) and 2 the cooler (secondary).

	H-group				G-group			
JD-2450000	v_1	$(O-C)_1$	v_2	$(O-C)_2$	v_1	$(O-C)_1$	v_2	$(O-C)_2$
5432.559 09	17.346	0.001	−48.742	0.057	16.954	0.014	−49.149	0.075
5467.507 40	−47.938	−0.010	16.282	−0.071	−48.140	0.016	15.823	−0.019
5468.492 96	−48.725	0.017	17.104	−0.062	−49.002	−0.035	16.582	−0.069
5470.485 28	−49.883	0.008	18.228	−0.086	−50.101	0.011	17.705	−0.088
5471.487 92	−50.220	−0.007	18.589	−0.046	−50.443	−0.011	18.086	−0.027
5477.661 39	−48.393	−0.037	16.770	−0.010	−48.645	−0.075	16.261	0.000
5478.664 94	−47.458	−0.013	15.852	−0.019	−47.663	−0.004	15.345	−0.009
5479.503 41	−46.618	−0.057	14.973	−0.015	−46.829	−0.054	14.495	0.022
5503.512 01	3.903	−0.030	−35.459	−0.041	3.570	−0.056	−35.968	−0.024
5504.506 35	5.859	−0.024	−37.428	−0.066	5.546	−0.023	−37.940	−0.055
5721.646 81	−29.487	0.073	−1.956	0.031	−29.733	0.140	−2.448	−0.022
5721.757 42	−29.746	0.063	−1.700	0.038	−30.050	0.073	−2.150	0.026
5722.656 25	−31.774	0.022	0.286	0.039	−32.106	−0.005	−0.199	0.000
5722.774 60	−32.030	0.023	0.557	0.054	−32.389	−0.032	0.095	0.037
5811.583 72	−32.927	0.029	1.471	0.067	−33.268	−0.006	0.972	0.009
5813.593 59	−37.061	−0.010	5.645	0.152	−37.374	−0.032	5.103	0.063
6137.544 67	18.418	0.020	−49.839	0.011	17.970	−0.021	−50.208	0.065
6138.529 70	18.009	0.002	−49.492	−0.032	17.557	−0.036	−49.896	−0.021
6178.631 70	−50.258	−0.038	18.669	0.027	−50.462	−0.018	18.151	0.026
6178.699 65	−50.229	0.006	18.687	0.030	−50.472	−0.014	18.183	0.043
6179.547 39	−50.351	0.006	18.768	−0.011	−50.556	0.019	18.274	0.018
6179.666 79	−50.354	0.010	18.782	−0.004	−50.545	0.037	18.295	0.032
6179.691 62	−50.374	−0.009	18.788	0.002	−50.603	−0.020	18.300	0.036
6214.498 23	10.895	0.013	−42.425	−0.074	10.573	−0.013	−42.901	−0.007
6240.545 79	−2.315	−0.054	−29.200	0.035	−2.614	0.088	−29.579	0.020
6448.947 01	−49.097	−0.002	17.506	−0.013	−49.285	0.003	16.964	−0.012

Table 3. Results of the orbital fit to the RVs performed by the H-group.

Parameter	Value	±
P (d)	88.3891	0.0008
T_Q (JD)[a]	2452 069.851	0.043
K_1 (km s^{-1})	34.524	0.010
K_2 (km s^{-1})	34.461	0.015
γ_1 (km s^{-1})	−15.846	0.008
$\gamma_2 - \gamma_1$ (km s^{-1})	0.177	0.015
$a_{12}\sin i$ (R$_\odot$)	120.549	0.036
e	0.0	(fix)
q	1.0018	0.0005
$M_1 \sin^3 i$ (M$_\odot$)	1.5020	0.0013
$M_2 \sin^3 i$ (M$_\odot$)	1.5047	0.0011
rms$_1$ (m s^{-1})	30	
rms$_2$ (m s^{-1})	54	
DOF[b]	43	
χ^2/DOF	0.9963	

Notes. [a]For a quadrature before the primary eclipse. Not adopted in further analysis. [b]Degrees of freedom.

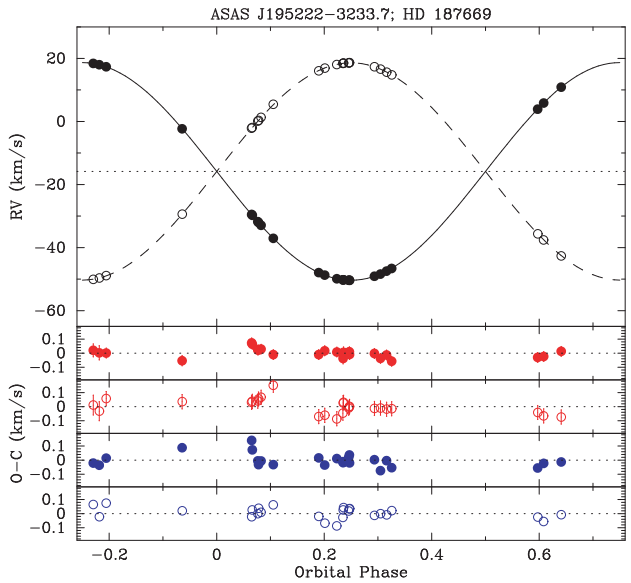

Figure 1. RV measurements and best-fitting orbital solution for ASAS-19. Solid line and filled symbols refer to the primary, and dashed line and open symbols to the secondary component. Differences in RV measurements by the two groups are smaller than the size of symbols, and the models are practically indistinguishable. The dotted line marks the systemic velocity of the primary. The difference between the two systemic velocities was accounted for. Lower panels depict the residuals for each component and each group (different fits) separately. Phase zero is set to the primary minimum. The resulting rms values are 30 and 54 m s^{-1} for the primary and secondary, respectively, from the H-group's solution (red), and 43 and 42 m s^{-1} analogously for the G-group (blue). A colour version of the figure is available in the online version of the manuscript.

component taken at the total primary eclipse. For disentangling and derivation of the atmospheric parameters, we used the LTE program MOOG (Sneden 1973) and followed the prescription given in Graczyk et al. (2014). Details of the method are given in Marino et al. (2008) and the line list in Villanova, Geisler & Piotto (2010). The totality spectrum was analysed first, and the temperature $T_{\rm eff,2} = 4360$ K was obtained. The disentangled spectra were scaled using the light ratio determined from the solution of RV and light

Table 4. Atmospheric parameters from MOOG (G-group).

Spectrum	$T_{\rm eff}$ (K)	$\log g$ (cgs)	[Fe/H] (dex)	v_t (km s^{-1})
Primary	4770	2.30	−0.25	1.25
Secondary	4440	1.60	−0.22	1.61
Totality	4360	1.57	−0.44	1.65
Adopted[a]	4360	1.90[b]	−0.30	1.65

Notes. [a]For the secondary. [b]From the WD solution.

Table 5. Atmospheric parameters from SME (H-group).

Spectrum	$T_{\rm eff}$ (K)	[Fe/H] (dex)	$v_{\rm rot}$ (km s^{-1})
Primary	4610	−0.24	6.87
Secondary	4310	−0.21	13.60
Totality	4290	−0.19	13.56
Adopted[a]	4300	−0.20	13.58

Note. [a]For the secondary, from 10 runs.

curves, assuming temperature $T_{\rm eff,2} = 4360$ K, by fitting, e.g., the temperature of the primary $T_{\rm eff,1}$. The light ratio varied from 2.2490 at 4670 Å to 2.6712 at 6470 Å. The results are summarized in Table 4. Typical errors in $T_{\rm eff}$, $\log g$, [Fe/H] and v_t are 70 K, 0.3, 0.15 dex and 0.2 km s^{-1}, respectively. For the uncertainties, parameters derived from the totality spectrum are consistent with those obtained from the disentangled spectrum of the secondary. The small differences at a level of 1σ are caused by a somewhat larger depth of the absorption lines in the disentangled spectrum.

The same procedure used for deriving $T_{\rm eff}$ here (methodology and data from HARPS), was used for Arcturus, a standard star with regards to $T_{\rm eff}$. It gave $T_{\rm eff} = 4290$ K (Villanova et al. 2010), which agrees very well with independent measurements (e.g. Ramírez & Allende Prieto 2011, which gives $T_{\rm eff} = 4286$ K). So, in spite of using an LTE approximation, we can recover a reliable $T_{\rm eff}$ for this kind of stars (cold giants at that metallicity), which is essentially free from larger systematic errors.

3.3.2 SME (H-group)

We also analysed the disentangled and total eclipse spectra with Spectroscopy Made Easy (SME) (Valenti & Piskunov 1996). To ensure that the disentangled spectra are properly scaled, we used the flux ratios obtained for each echelle order separately, taken from our initial TODCOR measurements. In the range of the V band they were in a good agreement with the flux ratio obtained from the JKTEBOP solution (next section). We also compared the scaled disentangled spectrum of the secondary with the spectrum in totality, and found an almost perfect match (Fig. 2).

We run SME separately on five HARPS orders between 5907 and 6215 Å, with $\log(g)$ being kept fixed to 2.507 and 1.907 for the primary and secondary, respectively – values found in the analysis are described in further sections. For a given component, all runs gave consistent values of $T_{\rm eff}$, [Fe/H] and v_{rot}, the last one being in agreement with the results expected from the measured radii, assuming spin–orbit alignment and rotational synchronization. As final results, we adopted average values of all five runs for the primary, and 10 (disentangled plus totality) for the secondary, and standard deviations as their uncertainties. We got $T_{\rm eff,1} = 4610 \pm 50$ K, $[{\rm Fe/H}]_1 = -0.24 \pm 0.12$ dex, $T_{\rm eff,2} = 4300 \pm 50$ K and $[{\rm Fe/H}]_2 = -0.20 \pm 0.07$ dex. Except $T_{\rm eff,1}$, all values are in a better than 1σ agreement with the ones adopted by the G-group (Table 4). However, the final value of $T_{\rm eff,1}$ by the G-group is somewhat lower (Section 3.5), and also consistent within 1σ with our SME analysis. We summarize our SME results in Table 5. Uncertainties of $v_{\rm rot}$ are 0.3 km s^{-1}.

Additionally, we estimated the secondary's effective temperature from the $V - I$ colour versus line-depth ratio calibrations by Strassmeier & Schordan (2000). We used the totality spectrum and measured 10 ratios of metallic lines from the 6380–6460 Å region, and got the intrinsic secondary's colour $(V_2 - I_2)_0 = 1.228 \pm 0.030$ mag. This corresponds to $T_{\rm eff,2} = 4370 \pm 80$ K (Worthey & Lee 2011), and a K2.5-3 III star (Tokunaga 2000).

3.4 Light-curve solution with JKTEBOP (H-group)

One of the codes we used for the light-curve analysis was version v28 of JKTEBOP (Southworth, Maxted & Smalley 2004a; Southworth et al. 2004b), which is based on the EBOP program (Popper & Etzel 1981). It is a fast procedure, working on one set of photometric data at a time. It does not analyse RV curves. On the basis of spectroscopic data, we first found the mass ratio and orbital period, which we included in the light-curve analysis. We found that the orbital period found directly by JKTEBOP is in agreement with the one from RVs, however, leading to a significantly worse orbital solution.

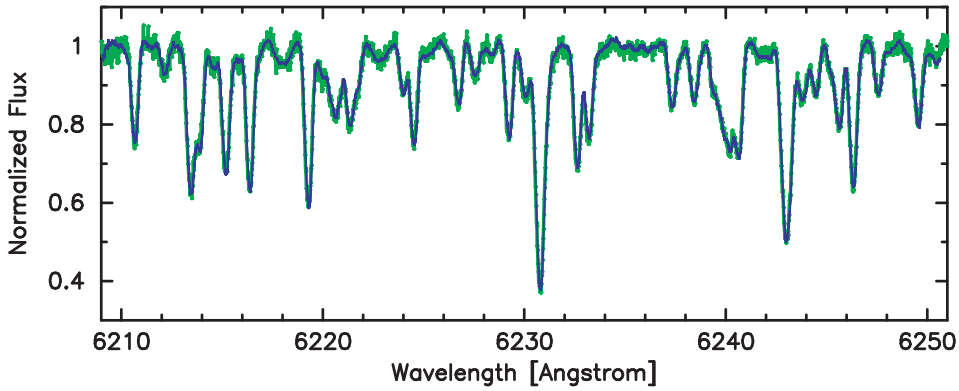

Figure 2. Comparison of the spectrum recorded during the total eclipse (green) with the rescaled secondary's spectrum from the disentangling (blue). The match is almost perfect, but the disentangled spectrum has much higher S/N. A colour version of the figure is available in the online version of the manuscript.

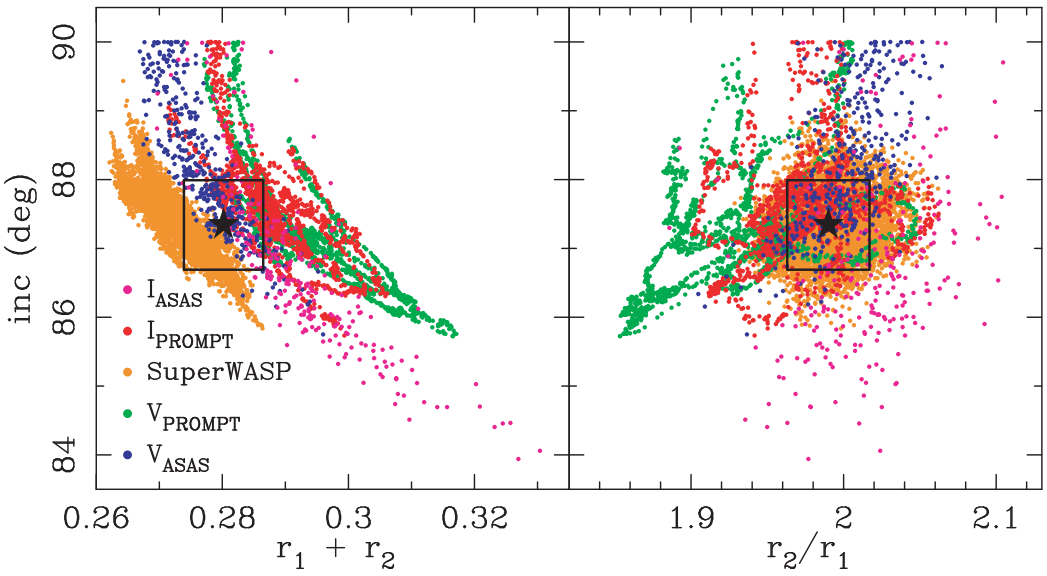

Figure 3. Results of the residual-shift analysis performed with JKTEBOP on all the data sets separately. Plots present the distribution of consecutive solutions on the $r_1 + r_2$ versus i (left) and $k = r_2/r_1$ versus i (right) panels. Black stars and boxes correspond to the adopted values with their 1σ uncertainties. The correlation between $r_1 + r_2$ and the inclination is clear; however, the inclination does not change significantly from set to set. A colour version of the figure is available in the online version of the manuscript.

This is because of a longer time span of spectroscopy with respect to PROMPT and SuperWASP observations, and that ASAS data do not have many points for the eclipses.

For JKTEBOP we used the logarithmic limb-darkening law with coefficients interpolated from the tables of van Hamme (1996) for ASAS and PROMPT. For the SuperWASP data, we used tables calculated by the developers of the PHOEBE code.[5] The gravity darkening coefficients and bolometric albedos were always kept fixed at the values appropriate for stars with convective envelopes ($g = 0.32$ and $A = 0.5$). As mentioned before, no significant eccentricity of the orbit of ASAS-19 was found, nor the third light, thus e and L_3 were kept fixed at 0. We fitted for the sum of the fractional radii $r_1 + r_2$, their ratio k, orbital inclination i, moment of the primary minimum T_0, surface brightness ratios J and brightness scales (out-of-eclipse magnitudes in each filter).

To calculate reliable errors, we run task 9, which uses the residual-shift method (Southworth 2008) to assess the importance of the correlated red noise, which is particularly strong in the SuperWASP data (Southworth et al. 2011). We run several tests to check how the final model varies with various limb-darkening coefficients and ephemeris, and we did not notice a strong dependence, but at least partially to account for limb-darkening coefficients and ephemeris uncertainties, we let them be perturbed in the residual-shift simulations. It is known that orbital inclination is correlated with the radii-related parameters, especially their sum. In Fig. 3 we show the results of the JKTEBOP analysis on $r_1 + r_2$ versus i and $k = r_2/r_1$ versus i diagrams. We see that different data sets give similar values of inclination and k, but clearly different areas of the $r_1 + r_2$ versus i plane are occupied. The most likely reason for this inconsistency is the activity and the location of spots, probably varying in time, which were not included in the JKTEBOP analysis. As shown for late-type dwarfs (for example: Różyczka et al. 2009; Windmiller 2010; Hełminiak et al. 2011), the location of spots on different components may lead to variations in the resulting radii reaching 2–3 per cent, while the accuracy of our photometry may not be sufficient to detect the spot-originated brightness variations.

For the resulting parameters, we adopted weighted averages of the values found from the five data sets. We mark them in Fig. 3, together with the adopted 1σ errors. The model light curves are presented in Fig. 4. Looking at the scatter of the PROMPT photometry for both eclipses, we can conclude that more spots reside on the primary (hotter, smaller) component. If so, the rms values of the H-group's RV measurements for both components are more likely enhanced by the rotational broadening than the activity. If it were activity, we would expect larger rms values for the (slower rotating) primary, but we observe the opposite. The resulting values of fractional radii $r_{1,2}$, and the inclination are given in Table 6. The oblateness of both components is below 1 per cent, so the use of JKTEBOP is justified.

Finally, we used the JKTEBOP solutions to derive observed $V - I$ colours of both components, and to estimate their effective temperatures. Note that these simple calculations are possible only for totally eclipsing systems. For the secondary, we simply used the photometry in the total eclipse and got 1.434(1) mag. Taking the intrinsic $(V_2 - I_2)_0 = 1.228(30)$ mag from line-depth ratios, we get $E(V - I) = 0.206(30)$ mag and $E(B - V) = 0.161(23)$, assuming $E(V - I) = 1.28\,E(B - V)$. From the light-curve solutions, we got magnitude differences between the components: $V_2 - V_1 = -0.959(23)$ and $I_2 - I_1 = -1.145(32)$ mag. We then get the observed primary's $V - I = 1.082(39)$ mag, and its intrinsic value of 1.046(39) mag. This corresponds to $T_{\rm eff,1} = 4710 \pm 110$ K (Worthey & Lee 2011) and a K0.5 III star (Tokunaga 2000). Interestingly, both temperatures obtained from the calibrations of Worthey & Lee (2011) – 4710 and 4370 K – are 1.7 per cent larger than those from our SME analysis (4630 and 4300 K).

3.5 Simultaneous radial velocity and light curve analysis with WD (G-group)

The G-group made a binary model using all data together at the same time. The code used in the analysis was the 2007 version

[5] http://phoebe-project.org/1.0/files/ld/swasp_2006.ld

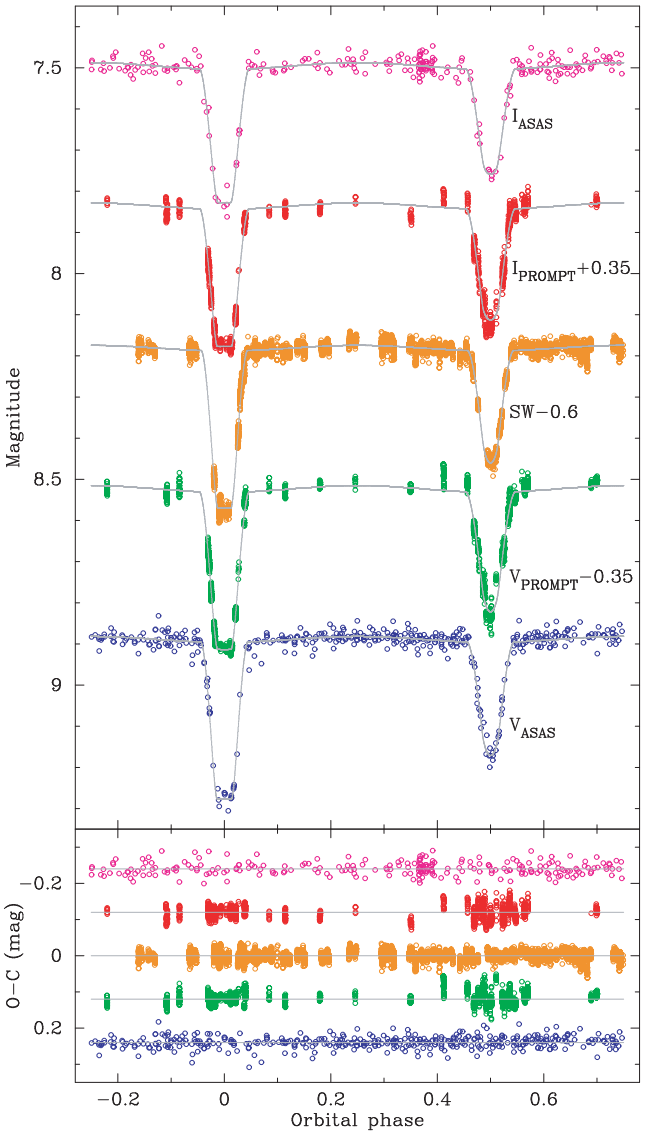

Figure 4. Top: Photometry of ASAS-19 (open circles) and JKTEBOP models (grey lines) for each band. PROMPT and SuperWASP data were shifted for clarity by the indicated values (in mag). Bottom: Residuals of the JKTEBOP models, shifted for clarity. Colour coding and sequence are the same as above. A colour version of the figure is available in the online version of the manuscript.

of the Wilson–Devinney program (Wilson & Devinney 1971; Wilson 1979, 1990; van Hamme & Wilson 2007). We simultaneously solved all light and RV curves. The light curves were divided into two groups: the visual group – containing all observations in the ASAS *V*-band, SuperWASP and PROMPT *V*-band data and the near-infrared group – containing ASAS *I*-band and PROMPT *I*-band data. Within both groups, some slight shifts were done to adjust SuperWASP and PROMPT magnitude scales to ASAS magnitudes. The differences in the mean depth and width of the eclipses between different data sets are smaller than the systematic effects (night-to-night variations) we noticed in the light curves. In total, the visual and near-infrared light curves contain 7121 and 1653 points, respectively. We used RVs derived from the broadening function analysis and we applied a shift of $+40$ m s^{-1} to the primary's velocities to account for its blue shift. The approach to find a model solution was essentially similar to the method described by Graczyk et al. (2014). The difference is that the primary's effective temperature was set as a free parameter instead of the secondary's one. The reason was that we estimated the unique surface temperature of the secondary component from an atmospheric analysis of the totality spectrum $T_2 = 4360 \pm 80$ K.

We set [Fe/H] $= -0.3$ from the atmospheric analysis with MOOG. The orbital period was kept as a free parameter of a solution. We assumed a circular orbit and synchronous rotation of both components. We also checked for the third light, but the fit resulted in negative values, thus we kept it fixed to zero. A logarithmic limb-darkening law was used (Klinglesmith & Sobieski 1970). In total, we adjusted 11 parameters in the model. The model light curves are presented in Fig. 5. The resulting parameters are shown in Table 7. We note that our effective temperatures are closer to the values from the Worthey & Lee (2011) calibrations obtained by the H-group, than to their SME results.

4 PHYSICAL PARAMETERS

4.1 G-group

Absolute values of parameters were calculated with the WD code, assuming the same astronomical constants as in table 5 of Graczyk et al. (2012). The distance to the system was derived using the di Benedetto (2005) calibration of visual surface brightness versus $(V - K)$ colour relation appropriate for giant stars and expressed in the Johnson photometric system. We used 2MASS magnitudes from Cutri et al. (2003): $J = 6.492$ mag and $K = 5.674$ mag, and extrapolated the components' light ratios in the *J*- and *K*-bands from the WD model: $l_{21}(J) = 3.26$ and $l_{21}(K) = 3.65$. The 2MASS

Table 6. Results of the JKTEBOP fit to the observed light curves (H-group).

Parameter	I_{ASAS}	V_{ASAS}	I_{PROMPT}	V_{PROMPT}	SuperWASP	Adopted
T_0 (JD-2452000)[a]	92.118(37)	92.036(47)	92.085(28)	92.095(30)	92.058(17)	92.074(25)
$r_1 + r_2$	0.2929(95)	0.2769(57)	0.2875(73)	0.2931(98)	0.2736(46)	0.2802(63)
$k = r_2/r_1$	2.014(44)	2.002(23)	1.975(29)	1.933(44)	1.992(22)	1.990(27)
i (deg)	86.5(1.2)	88.0(1.1)	87.52(62)	87.20(79)	87.30(46)	87.34(65)
r_1	0.0971(40)	0.0923(24)	0.0967(31)	0.0999(49)	0.0914(18)	0.0937(23)[b]
r_2	0.1958(62)	0.1847(34)	0.1909(44)	0.1932(54)	0.1821(30)	0.1865(59)[b]
$(L_2/L_1)_I$	2.934(93)	–	2.822(82)	–	–	2.871(87)
$(L_2/L_1)_V$	–	2.421(43)	–	2.413(78)	–	2.419(51)
$(L_2/L_1)_{SW}$	–	–	–	–	2.404(27)	2.404(27)
rms (mag)	0.025	0.017	0.017	0.017	0.011	

Notes. [a]Mid-time of the primary eclipse. [b]From the adopted sum and ratio of radii.

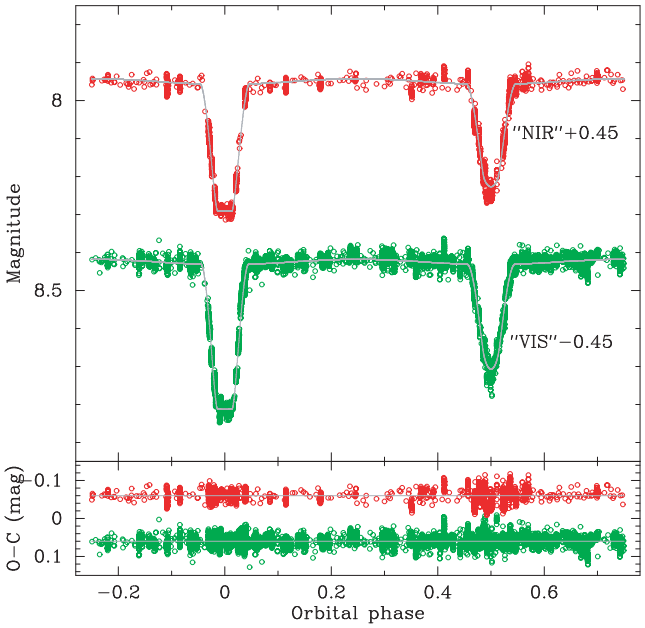

Figure 5. Same as Fig. 4 but for WD models, and combined visual and near-infrared light curves. A colour version of the figure is available in the online version of the manuscript.

Table 7. Results of the WD fit (G-group).

Parameter	Primary	Secondary
$P_{\rm obs}$ (d)	88.3865(27)	
T_0 (JD-2452000)	92.034(97)	
a ($R_\odot$)	120.51(4)	
q	1.0004(5)	
i (deg)	87.68(15)	
γ (km s^{-1})	−16.19(1)	−16.15(1)
Ω^a	11.629(77)	6.323(19)
r	0.0941(7)	0.1887(7)
$T_{\rm eff}$ (K)	4687(5)	4360^b
L_V	3.607(7)	8.956(16)
L_I	3.237(6)	9.307(16)
K (km s^{-1})	34.458(15)	34.444(15)
RV rms (m s^{-1})	43	42
V-band rms (mag)	0.008	
I-band rms (mag)	0.016	
DOF	8815	
χ^2/DOF	0.991	

Notes. ^{a}Dimensionless equipotential of the Roche model. ^{b}Fixed.

magnitudes were converted on to Johnson's system using equations given by Bessell & Brett (1988) and Carpenter (2001).[6] The interstellar reddening was derived from reddening maps (Schlegel, Finkbeiner & Davis 1998) using normalization given by Schlafly & Finkbeiner (2011), assuming a distance to our target (see below) and Galactic dust distribution consistent with the thin disc model from Drimmel & Spergel (2001). The resulting $E(B-V) = 0.121 \pm 0.016$, where the error takes into account the uncertainty of total extinction from Schlegel et al. (1998) maps and the Milky Way's thin disc model parameters. The *BC*'s were calculated from the Alonso, Arribas & Martínez-Roger (1999) calibration for a given effective temperature. The derived extinction is almost equal to the extinction estimated by the H-group, which puts confidence in our approach and resulting distance of 614 ± 18 pc. The distance corresponds to a parallax of 1.63 ± 0.05 mas.

4.2 H-group

Absolute values of parameters and their uncertainties were calculated with the JKTABSDIM code, available together with JKTEBOP, assuming astronomical constants suggested by Harmanec & Prša (2011).[7] This simple code combines the spectroscopic and light curve solutions to derive a set of stellar absolute dimensions, related quantities and distance. We used photometry from 2MASS in *JHK* ($J = 6.492$, $H = 5.674$ and $K = 5.674$ mag), from Tycho (Høg et al. 2000) in B (10.13 mag), and out-of-eclipse combined Johnson's V magnitude from the JKTEBOP solution (8.866 mag). JKTABSDIM calculates distances using a number of bolometric corrections for various filters (Bessell, Castelli & Plez 1998; Flower 1996; Girardi et al. 2002) and surface brightness versus $T_{\rm eff}$ relations from Kervella et al. (2004) – 13 in our case. We found $E(B-V)$ for which the standard deviation of the resulting distance (assumed to be its uncertainty) is the lowest. Outside the given error of $E(B-V)$, distances differ from each other by more than 1σ. The result – 0.13(7) mag – is in a good agreement with the one found on the basis of the secondary's $V-I$ colours – 0.16(2) mag. Employing this value, and temperatures from calibrations of Worthey & Lee (2011) – 4710 and 4370 K – we get a very similar distance of 604(18) pc.

4.3 Adopted parameters

We combined the results from the analysis done by our two groups to derive absolute parameters. A comparison of the two approaches is presented in Table 8, and the final set of physical parameters in Table 9. As final values, we adopted straight averages of the two obtained by the two groups. To get conservative errors, we took the average of the two uncertainties and added it in quadrature to half of the difference between the two values. When systematic errors were not included [R and $\log(g)$], we assumed that they are 2 × the uncertainty given. All in all, we reached a very good precision in radii (2.5 + 2.2 per cent), and one of the best estimates of stellar masses in the literature (0.27 + 0.27 per cent). We have also calculated the distance to the system with 3.3 per cent error (total systematic and statistical uncertainty), which translates into 0.05 mas uncertainty in parallax at 606 pc (1.65 mas). Having precisely measured distances on such scales will be important in independently verifying the results of the recently launched *Gaia* mission.

5 DISCUSSION

5.1 Galactic binaries with giant components

In the online DEBCat catalogue[8] there are only 17 systems listed that have at least one star evolved and larger than 5 $R_\odot$, and both

[6] http://www.astro.caltech.edu/~jmc/2mass/v3/transformations/

[7] The disparities obtained from using two different sets of constants are in this case negligible in comparison with the uncertainties of the derived physical parameters.

[8] http://www.astro.keele.ac.uk/~jkt/debcat/

Table 8. Comparison of used approaches. For each method a main advantage and presumable source of systematic errors is given.

	G-group			H-group		
Analysis stage	Method	Advantages	Systematic errors	Method	Advantages	Systematic errors
RV derivation	RaVeSpAn	Direct determination from BF	Templates	Tomography and least-squares fitting	Disentangled spectra	Initial template mismatch
Atmospheric	MOOG	Well calibrated against temperature temperature standards	LTE	SME and line-depth ratios	Line profiles fitting, also blends	LTE
Light curves	WD	All light curves simultaneously	Fluxes from LTE models; activity	JKTEBOP	Fast; red noise accounted for	Stellar activity
RV curves	WD	Tidal corrections included	Relativistic effects not included	V2FIT	Relativistic eff- ects included	Tidal corrections not included
Distance	SB – colour relation	Direct, empirical	SB calibration	JKTABSDIM	Average of various methods	Calibration of the methods used

Table 9. Physical parameters of the system.

	G-group[a]		H-group[b]		Adopted	
Parameter	Primary	Secondary	Primary	Secondary	Primary	Secondary
Spectrum	K0 III[c]	K2.5 III[c]	K0.5 III[d]	K2.5-3 III[d]	K0-0.5 III	K2.5 III
M ($M_\odot$)	1.501(2)	1.502(2)	1.507(3)	1.509(3)	1.504(4)	1.505(4)
R ($R_\odot$)	11.34(9)	22.74(9)	11.31(28)	22.50(71)	11.33(28)	22.62(50)
log g (cgs)	2.505(6)	1.901(3)	2.509(21)	1.913(27)	2.507(20)	1.907(19)
$T_{\rm eff}$ (K)	4687(85)	4360(80)	4610(50)[e]	4300(50)[e]	4650(80)	4330(70)
L ($L_\odot$)	55.7(4.1)	168(12)	51.9(3.3)	155(12)	53.9(3.9)	161(13)
$M_{\rm bol}$ (mag)	0.39	−0.81	0.46	−0.72	0.42	−0.77
BC_V (mag)	−0.48	−0.71	−0.44	−0.66	−0.46	−0.69
[Fe/H]	−0.25(15)	−0.30(15)	−0.24(12)	−0.20(7)	−0.25(10)	
Distance (pc)	614(18)		598(18)		606(18)	
$E(B-V)$ (mag)	0.12(2)		0.13(7)		0.13(5)	

Notes. [a]Formal WD fit errors; systematic errors not always included. [b]Systematic errors included. [c]According to calibration by Alonso et al. (1999). [d]According to calibration by Tokunaga (2000). [e]From the SME analysis.

masses and radii known with an accuracy of 2 per cent or better. Of these, only three are Galactic systems (others belong to the LMC or Small Magellanic Cloud) and only the primaries are larger than 5 $R_\odot$. These are V380 Cyg (B1.5 III; Tkachenko et al. 2014), TZ For (Andersen et al. 1991) and KIC 8410637 (Frandsen et al. 2013). A number of other Galactic systems have smaller components, although they evolved from the main sequence (AI Phe, Andersen et al. 1988, Hełminiak et al. 2009; CF Tau, Lacy, Torres & Claret 2012; V432 Aur, Siviero et al. 2004), or are much more evolved but measured less precisely (OW Gem, Gałan et al. 2008; α Aur, Torres, Claret & Young 2009; ASAS J182510-2435.5 and V1980 Sgr, Ratajczak et al. 2013). This makes ASAS-19 the best measured, evolved Galactic binary, and a very unique object, important for studies of the late stages of stellar evolution.

5.2 Age and evolutionary status

Both stars are currently on the red giant branch, but before the Red Clump (Fig. 6). At this stage of evolution, stars of a similar mass present a wide range of radii, temperatures, luminosities etc., so precise mass and metallicity determination is crucial to constrain their age and exact evolutionary phase. We compared our results in Table 9 with stellar isochrones from the Padova and Trieste Stellar Evolution Code (PARSEC) (Bressan et al. 2012). We used the value of [Fe/H] = −0.25, which for this set translates into

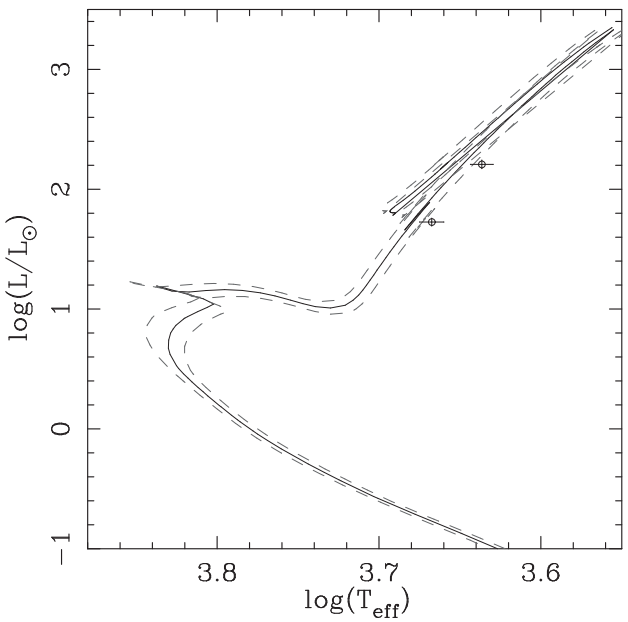

Figure 6. Location of ASAS-19 on a Hertzsprung-Russell diagram. The black line is the isochrone for [Fe/H] = −0.25 and 2.38 Gyr. Two grey dashed lines are isochrones for [Fe/H] = −0.15, 2.55 Gyr (colder), and [Fe/H] = −0.35, 2.24 Gyr (hotter).

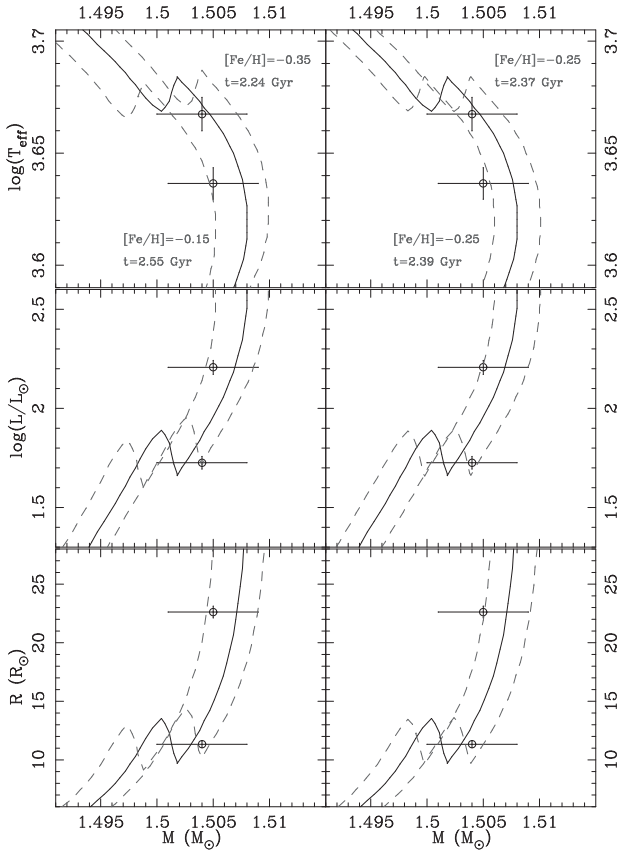

Figure 7. Comparison of our final results with a 2.38 Gyr, [Fe/H] = −0.25 isochrone from the PARSEC set (black solid line). Other, marginally fitting isochrones are plotted in grey (dashed): on the left panels for (τ, [Fe/H]) = (2.55 Gyr, −0.15), and (2.24 Gyr, −0.35), showing the age uncertainty due to metallicity, and on the right panels for (τ, [Fe/H]) = (2.37 Gyr, −0.25), and (2.39 Gyr, −0.25), showing the age uncertainty due to mass.

$Z = 0.00855$ and $Y = 0.2642$. We looked for the age that fits best to our precise and direct mass measurements, and found that ASAS-19 is $2.38^{+0.17}_{-0.14}$ Gyr old. Most of the uncertainty in its age comes from the [Fe/H] determination – for a fixed metal content, the uncertainty from the mass determination is only 0.01 Gyr.

In Fig. 7 we show our results on mass versus temperature, luminosity and radius diagrams, together with various isochrones: the best fitting (2.38 Gyr, −0.25 dex); two for the marginal values of age and metallicity that still reproduce our results within 1σ, 2.24 Gyr for −0.35, and 2.55 Gyr for −0.15 dex (left, also in Fig. 6); and two more for fixed metallicity of −0.25 dex but ages of 2.37 and 2.39 Gyr (right). Note that the 2.38 Gyr, −0.25 dex isochrone that fits the mass measurements best, predicts slightly hotter and more luminous stars (Fig. 6). This discrepancy may come from either metallicity or temperatures being a bit underestimated. The 2.38 Gyr, −0.25 dex isochrone fits better if temperatures from the calibrations of Worthey & Lee (2011) are used.

5.3 Usefulness of observations during total eclipses

Cases like ASAS-19 allow for independent verification of indirect approaches to determining the physical parameters of stars in eclipsing binaries. It shows how the observations performed during a total eclipse are useful for the analysis of DEBs. Especially important was the spectrum taken when only one star was visible. From its analysis, we could independently estimate the temperature of one of the components and the metallicity of the whole system. Light curves alone do not constrain well the temperature scale, only the ratio of the two $T_{\rm eff}$'s. The common approach to light-curve modelling utilizes the observed colour of the whole system, but it works fine only if the components have similar temperatures or the total light is dominated by one of them, and only if the observed colour is properly dereddened. In our case, we could securely keep one of the $T_{\rm eff}$'s fixed. We could also calculate the observed colours of both stars, one directly from the photometry of the total eclipse, and the other from simple calculations described in Section 3.4. Having the multi-band photometry and the $T_{\rm eff}$ estimation from the spectrum, one can also calculate $E(B-V)$ by comparing the colours observed and predicted by colour–temperature calibrations. For nearby systems, where interstellar extinction is not significant, the observed colours would be enough to calculate the temperature of both components.

We also used the totality spectrum to estimate the metallicity of the system. This helped us to constrain the age of the binary. The well-known age–metallicity degeneration is weaker for red giants than for main sequence stars, but is still present. As we showed in Section 5.2, 0.1 dex uncertainty in [Fe/H] translates into 0.1 Gyr error in age. For main sequence objects, it is at least 10 times more, but it would still be enough to discriminate between stars that have just started their main sequence evolution, and those that are about to finish it soon.

Metallicity can also be estimated from tomographically disentangled spectra, but the disentangled spectra have to be correctly renormalized to account for the companion's continuum, which dilutes the depth of the absorption lines. This is relatively easy for systems with total eclipses, as from the depth of the eclipse it is straightforward to calculate the contribution of each component, and it also allows us to check if the flux ratio inferred from TODCOR is correct. It is also possible to verify the results of decomposition by comparing the decomposed and totality spectra, as in Fig. 2. As one can see, the disentangled spectra have higher S/N; however, the approach we used (H-group) requires at least eight observations in evenly spread orbital phases. For totally eclipsing systems, having a single observation during the total eclipse is less time-consuming and can give important results with less effort. We also want to note, that the decomposition itself is easier, as for each observed composite spectrum, only two parameters are required: the velocity difference for the component visible in totality and the flux ratio, both of which can be estimated separately or are easy to fit for.

Finally we want to emphasize that a high signal-to-noise spectrum taken during totality can also be a very good template for RV measurements of at least one component, as it obviously matches its $T_{\rm eff}$, $\log g$, [Fe/H] and turbulence velocities.

ACKNOWLEDGEMENTS

We would like to thank the staff of the European Southern Observatory La Silla observatory for their support during observations, and the anonymous referee for valuable comments and suggestions, which helped to improve this work.

KGH acknowledges support provided by the National Astronomical Observatory of Japan as Subaru Astronomical Research Fellow and the Polish National Science centre (grant 2011/03/N/ST9/01819). We (DG, BP, GP, PK and KS) gratefully acknowledge financial support for this work from the Polish National Science Centre (grant 2013/09/B/ST9/01551) and the TEAM subsidy from the Foundation for Polish Science. DG, GP

and WG are supported by the BASAL Centro de Astrofisica y Tecnologias Afines (PFB-06/2007). DG and WG also acknowledge support from the Millennium Institute of Astrophysics of the Iniciativa Cientifica Milenio del Ministerio de Economia, Fomento y Turismo de Chile (project IC120009). SV gratefully acknowledges the support provided by Fondecyt (register number 1130721). MK is supported by a European Research Council Starting Grant, the Polish National Science Centre (grant 5813/B/H03/2011/40), the Ministry of Science and Higher Education (grant W103/ERC/2011) and the Foundation for Polish Science through grant 'Ideas for Poland'. MR is supported by the Polish National Science Centre (grant 2011/01/N/ST9/02209). This research was supported in part by the National Science Foundation (grants 0959447, 0836187, 0707634 and 0449001), and by the European Social Fund and the national budget of the Republic of Poland within the Integrated Regional Operational Programme, Measure 2.6, Regional Innovation Strategies and Transfer of Knowledge – An Individual Project of the Kuyavian-Pomeranian Voivodship 'Scholarships for PhD Students 2008/2009 – IROP'.

We have used data from the WASP public archive in this research. The WASP consortium comprises the University of Cambridge, Keele University, University of Leicester, The Open University, The Queens University Belfast, St Andrews University and the Isaac Newton Group. Funding for WASP comes from the consortium universities and from the UK's Science and Technology Facilities Council.

REFERENCES

Alonso A., Arribas S., Martínez-Roger C., 1999, A&AS, 140, 261
Andersen J., Clausen J. V., Nordström B., Gustaffson G., Vandenberg D. A., 1988, A&A, 196, 128
Andersen J., Clausen J. V., Nordström B., Tomkin J., Mayor M., 1991, A&A, 246, 99
Baines E. K., Armstrong J. T., Schmitt H. R., Benson J. A., Zavala R. T., van Belle G. T., 2014, ApJ, 781, 90
Bedding T. R. et al., 2010, ApJ, 713, 176
Bessell M. S., Brett J. M., 1988, PASP, 100, 1134
Bessell M. S., Castelli F., Plez B., 1998, A&A, 333, 231
Bressan A., Marigo P., Girardi L., Salasnich B., Dal Cero C., Rubele S., Nanni A., 2012, MNRAS, 427, 127
Carpenter J. M., 2001, AJ, 121, 2851
Coelho P., Barbuy B., Meléndez J., Schiavon R. P., Castilho B. V., 2005, A&A, 443, 735
Cutri R. M. et al., 2003, VizieR, Online Data Catalogue, 2246, 0
di Benedetto G. P., 2005, MNRAS, 357, 174
Drimmel R., Spergel D. N., 2001, ApJ, 556, 181
Flower P. J., 1996, ApJ, 469, 355
Frandsen S. et al., 2013, A&A, 556, A138
Gałan C., Mikołajewski M., Tomov T., Kolev D., Graczyk D., Majcher A., Janowski J. L., Cikała M., 2008, Observatory, 128, 298
Girardi L., Bertelli G., Bressan A., Chiosi C., Groenewegen M. A. T., Marigo P., Salasnich B., Weiss A., 2002, A&A, 391, 195
Graczyk D. et al., 2012, ApJ, 750, 140
Graczyk D. et al., 2014, ApJ, 780, 59
Harmanec P., Prša A., 2011, PASP, 123, 976
Hełminiak K. G., Konacki M., Ratajczak M., Muterspaugh M. W., 2009, MNRAS, 400, 969
Hełminiak K. G. et al., 2011, A&A, 527, A14
Houk N., 1982, Michigan Catalogue of Two-dimensional Spectral Types for the HD stars. Volume 3. Declinations −40 deg to −26 deg
Høg E. et al., 2000, A&A, 355, L27
Kallinger T., Weiss W. W., De Ridder J., Hekker S., Barban C., 2009, ASPC, 404, 307
Kervella P., Thévenin F., Di Folco E., Ségransan D., 2004, A&A, 426, 297
Klinglesmith D. A., Sobieski S., 1970, AJ, 75, 175
Konacki M., Muterspaugh M. W., Kulkarni S. R., Hełminiak K. G., 2010, ApJ, 719, 1293
Lacy C. H. S., Torres G., Claret A., 2012, AJ, 144, 167
Marino A. F. et al., 2008, A&A, 490, 62
Mayor M. et al., 2003, The Messenger, 114, 20
Pietrzyński G. et al., 2013, Nature, 495, 76
Pilecki B., Konorski P., Górski M., 2012, Proc. IAU Symp. 282, From Interacting Binaries to Exoplanets. p. 301
Pojmański G., 2002, Acta Astron, 52, 397
Pollacco D. L. et al., 2006, PASP, 118, 1407
Popper D. M., Etzel P. B., 1981, AJ, 86, 102
Porter D. H., Woodward P. R., 2000, ApJS, 127, 159
Ramírez I., Allende Prieto C., 2011, ApJ, 743, 135
Ratajczak M., Hełminiak K. G., Konacki M., Jordán A., 2013, MNRAS, 433, 2357
Różyczka M., Kałużny J., Pietrukowicz P., Pych W., Mazur B., Catelán M., Thompson I. B., 2009, Acta Astron, 59, 385
Rucinski S. M., 1992, AJ, 104, 1968
Rucinski S. M., 1999, in Hearnshaw J. B., Scarfe C. D., eds, Astronomy Society of the Pacific Conference Series Vol. 185, IAU Colloquium 170, Precise Stellar Radial Velocities. Astron. Soc. Pac., San Francisco, p. 82
Schlafly E. F., Finkbeiner D. P., 2011, ApJ, 737, 103
Schlegel D. J., Finkbeiner D. P., Davis M., 1998, ApJ, 500, 525
Schwarzschild M., 1975, ApJ, 195, 137
Siviero A., Munari U., Sordo R., Dallaporta S., Marrese P. M., Zwitter T., Milone E. F., 2004, A&A, 417, 1083
Sneden C., 1973, ApJ, 184, 839
Southworth J., 2008, MNRAS, 386, 1644
Southworth J., Maxted P. F. L., Smalley B., 2004a, MNRAS, 351, 1277
Southworth J., Zucker S., Maxted P. F. L., Smalley B., 2004b, MNRAS, 355, 986
Southworth J., Pavlovski K., Tamajo E., Smalley B., West R. G., Anderson D. R., 2011, MNRAS, 414, 3740
Strassmeier K. G., Schordan P., 2000, Astron. Nachr., 321, 277
Tkachenko A. et al., 2014, MNRAS, 438, 3093
Tokunaga A. T., 2000, in Cox A. N., ed., Allen's Astrophysical Quantities, 4th edn. Springer-Verlag, New York, p. 143
Torres G., Claret A., Young P. A., 2009, ApJ, 700, 1349
Torres G., Andersen J., Gimenez A., 2010, A&A Rev., 18, 67
Valenti J. A., Piskunov N., 1996, A&AS, 118, 595
van Hamme W., 1996, AJ, 106, 2096
van Hamme W., Wilson R. E., 2007, ApJ, 661, 1129
Villanova S., Geisler D., Piotto G., 2010, ApJ, 722, 18
Wilson R. E., 1979, ApJ, 234, 1054
Wilson R. E., 1990, ApJ, 356, 613
Wilson R. E., Devinney E. J., 1971, ApJ, 166, 605
Windmiller G., Orosz J. A., Etzel P. B., 2010, ApJ, 712, 1003
Worthey G., Lee H.-C., 2011, ApJS, 193, 1
Zucker S., Mazeh T., 1994, ApJ, 420, 806

SUPPORTING INFORMATION

Additional Supporting Information may be found in the online version of this article:

Table 1. The PROMPT *V*, *I* and ASAS *I* photometry of ASAS-19 (http://mnras.oxfordjournals.org/lookup/suppl/doi:10.1093/mnras/stu2680/-/DC1).

Please note: Oxford University Press are not responsible for the content or functionality of any supporting materials supplied by the authors. Any queries (other than missing material) should be directed to the corresponding author for the article.

This paper has been typeset from a TEX/LATEX file prepared by the author.